frontiers | Frontiers in Chemistry

TYPE Original Research
PUBLISHED 25 January 2023
DOI 10.3389/fchem.2023.1138932

OPEN ACCESS

EDITED BY
Edison Huixiang Ang,
Nanyang Technological University, Singapore

REVIEWED BY
Jixin Zhu,
University of Science and Technology of China, China
Xiaohui Song,
Hefei University of Technology, China

*CORRESPONDENCE
Wenjia Xu,
xwj0729@126.com
Yuhua Feng,
ias_yhfeng@njtech.edu.cn

†These authors have contributed equally to this work

SPECIALTY SECTION
This article was submitted to Nanoscience, a section of the journal Frontiers in Chemistry

RECEIVED 06 January 2023
ACCEPTED 16 January 2023
PUBLISHED 25 January 2023

CITATION
Zhang J, Ren Q, Wang Y, Xiao R, Chen H, Xu W and Feng Y (2023), Diffusion-controlled bridging of the Au Island and Au core in Au@Rh(OH)$_3$ core-shell structure. *Front. Chem.* 11:1138932.
doi: 10.3389/fchem.2023.1138932

Diffusion-controlled bridging of the Au Island and Au core in Au@Rh(OH)$_3$ core-shell structure

Jie Zhang[1†], Quan Ren[1†], Yun Wang[1], Ruixue Xiao[1], Hongyu Chen[1,2], Wenjia Xu[1,3]* and Yuhua Feng[1]*

[1]Institute of Advanced Synthesis, School of Chemistry and Molecular Engineering, Nanjing Tech University, Nanjing, China, [2]School of Science, Westlake University, Hangzhou, China, [3]School of Physical and Mathematical Science, Nanjing Tech University, Nanjing, China

Hybrid nanostructures have garnered considerable interest because of their fascinating properties owing to the hybridization of materials and their structural varieties. In this study, we report the synthesis of [Au@Rh(OH)$_3$]-Au island heterostructures using a seed-mediated sequential growth method. Through the thiol ligand-mediated interfacial energy, Au@Rh(OH)$_3$ core-shell structures with varying shell thicknesses were successfully obtained. On these Au@Rh(OH)$_3$ core-shell seeds, by modulating the diffusion of $HAuCl_4$ in the porous Rh(OH)$_3$ shell, site-specific growth of Au islands on the inner Au core or on the surface of the outer Rh(OH)$_3$ shell was successfully achieved. Consequently, two types of distinct structures, the Au island-on-[Au@Rh(OH)$_3$] dimer and Au island-Au bridge-[Au@Rh(OH)$_3$] dumbbell structures with thin necks were obtained. Further modulations of the growth kinetics led to the formation of Au plate-Au bridge-[Au@Rh(OH)$_3$] heterostructures with larger structural anisotropy. The flexible structural variations were demonstrated to be an effective means of modulating the plasmonic properties; the Au–Au heterostructures exhibited tunable localized surface plasmon resonance in the visible-near-infrared spectral region and can be used as surface-enhanced Raman scattering (SERS) substrates capable of emitting strong SERS signals. This diffusion-controlled growth of Au bridges in the Rh(OH)$_3$ shells (penetrating growth) is an interesting new approach for structural control, which enriches the tool box for colloidal nanosynthesis. This advancement in structural control is expected to create new approaches for colloidal synthesis of sophisticated nanomaterials, and eventually enable their extensive applications in various fields.

KEYWORDS

core-shell, plasmonic structure, LSPR coupling, spacing layer, SERS

1 Introduction

The growth of crystals in a structure inevitably occupies the internal space (Li et al., 2009; Crossland et al., 2013; Shen et al., 2018). When the growth reaches a certain level, it penetrates the material and grows outside the structure. The penetration phenomenon originating from the mechanical force of the crystal growth is common in nature. For instance, in biomineralization (Tampieri et al., 2011; Campodoni et al., 2018; Chen et al., 2019), the growth of biominerals can be divided into two stages: the 1st stage; growth in the tissues, and the 2nd stage; growth outside after penetrating the interface. In lithium batteries, the layered growth of Li can transform into dendrites, and their overgrowth may penetrate the battery membrane, resulting in a short circuit or destruction of the battery structure (Bai et al., 2018; Wang et al., 2019b; Wang et al., 2021; Yang et al., 2022).

10.3389/fchem.2023.1138932

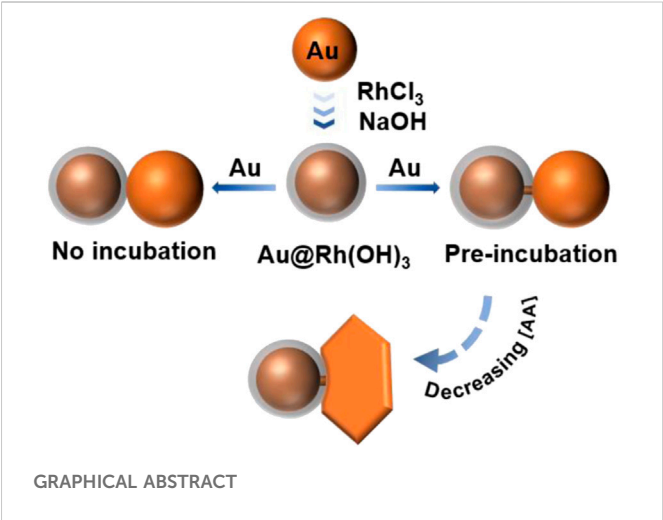

GRAPHICAL ABSTRACT

The nature of the above phenomena is the overgrowth of new domains at the nanoscale, which eventually leads to the penetration of the interface. In contrast to the result under an applied force, growth-induced penetration is a synergistic effect controlled by multiple factors. Therefore, understanding the laws and mechanisms of growth penetration would be helpful in studying these macroscopic phenomena.

The main challenge of this type of study is the difficulty in controlling the initial growth site and characterizing the growth process in detail. Thus, a suitable model system is very significant in the study of the growth penetration phenomena.

In our previous study, the growth of Ag on the surface of the Ag seeds in the Poly (styrene-b-acrylic acid) (PSPAA) shell (Jiang et al., 2018) was achieved. The continuous extrusion of the PSPAA polymer with Ag growth eventually led to the penetration of the polymer shell. The growth of the Ag outside the polymer shell led to the wrapping of seeds by the Ag nanoplate with a long and narrow nanogap. We speculate that the penetration of the Ag bridge is due to the porous nature of the PSPAA shell after the swelling-deswelling process. The growth of Ag continuously occupied the pores in the PSPAA and eventually penetrated out. Because of the mobility of the PSPAA shell, it is difficult to study the penetration of the PSPAA shell owing to the overgrowth of Ag in the shell.

Herein, we report that the penetration growth of Au was achieved in the hard porous $Rh(OH)_3$ layer in Au@$Rh(OH)_3$ core-shell structures. Specifically, through interfacial energy control, uniform concentric Au@$Rh(OH)_3$ core-shell structures with varying shell thicknesses were successfully synthesized (Figure 1) and used as seeds for the growth of Au–Au heterostructures. Controlling the diffusion of the $HAuCl_4$ precursor in the $Rh(OH)_3$ shells led to the formation of two types of Au–Au hybrids: Au island-on-[Au@$Rh(OH)_3$] dimer and Au island-Au bridge-[Au@$Rh(OH)_3$] dumbbell structures (Figure 2). Interestingly, by tuning the growth kinetics, Au plate-Au bridge-[Au@$Rh(OH)_3$] dumbbell structures were also obtained (Figures 3, 4). With structural variations, the localized surface plasmon resonance (LSPR) and surface-enhanced Raman scattering (SERS) of the Au–Au heterostructures exhibited excellent responses, thus providing a new method for LSPRs tuning for plasmonic applications.

2 Experimental section

2.1 Materials and methods

All the chemical reagents were used as purchased without further purification. Hydrogen tetrachloroaurate (III) hydrate ($HAuCl_4{\cdot}3H_2O$), 99.9% (metal basis Au 49%), trisodium citrate dihydrate (99%) was purchased from Alfa Aesar; 2-mercapto-5-benzimidazolecarboxylic acid (MBIA) (97%), rhodium (III) chloride trihydrate (98%), ascorbic acid (99%) was purchased from Aladdin; and polyvinyl pyrrolidone (average Mw 29000) was purchased from Aldrich. Absolute ethanol and deionized water (DI) (18.3 MΩ) were used for all solution preparations.

2.2 Characterizations

Transmission electron microscopy (TEM) images were obtained using an FEI Talos L120C microscope operated at 120 kV. Scanning electron microscopy (SEM) measurements were performed using a Quanta 250 FEG scanning electron microscope. High resolution TEM (HRTEM) was performed using a JEOL JEM-2100 transmission electron microscope operated at 200 kV. Ultraviolet-visible-near-infrared spectra were collected on a Lambda 750 ultraviolet-visible spectrophotometer. SERS was measured using a portable Raman analyzer (Accuman SR-510Pro) equipped with a 785 nm laser (350 mW) using as-synthesized sample solutions in a cuvette (1 cm optical path). The integration time was set at 10 s for all samples. X-ray photoelectron spectroscopy (XPS) spectra were collected using a Thermo SCIENTIFIC ESCALAB 250Xi photoelectron spectrometer equipped with a monochromatic Al Kα source (E = 1487.20 eV). Thermogravimetric analyses [thermal gravity (TG)/derivative thermogravimetry (DTG)] were performed using a TGA 2-1100SF thermal gravimetric analyzer.

2.3 Synthesis of Au–Au homometallic heterostructures

2.3.1 Synthesis of Au@$Rh(OH)_3$ core-shell nanoparticles

In a typical synthesis, the as-synthesized citrate-stabilized Au nanospheres (48 nm in diameter, Figure 1A) were incubated with the MBIA ligand at 60°C for 2 h. After cooling to room temperature (RT), different amounts of $RhCl_3$ (10 mM) were added to the above solution under vigorous vortexing, followed by heating in an oven at 100°C for 15 min. Subsequently, 200 µl of the product was separated through centrifugation at 3,500 rpm for 10 min. The concentrated NPs collected at the bottom of the centrifuge tube were directly used in the TEM/SEM characterization. The other 500 µl of the as-synthesized sample was incubated with 2 µL of 10 mM 2-naphthalenethiol ligand at 60°C for 2 h and thereafter used for SERS measurement. The remaining 300 µl was diluted five times for absorption spectrum collection.

2.3.2 Synthesis of Au Island-Au Bridge-[Au@$Rh(OH)_3$] dumbbell structures

For the synthesis of Au–Au hybrid nanostructures, Au–Rh $(OH)_3$ core-shell NPs with varying shell thicknesses were used as seeds,

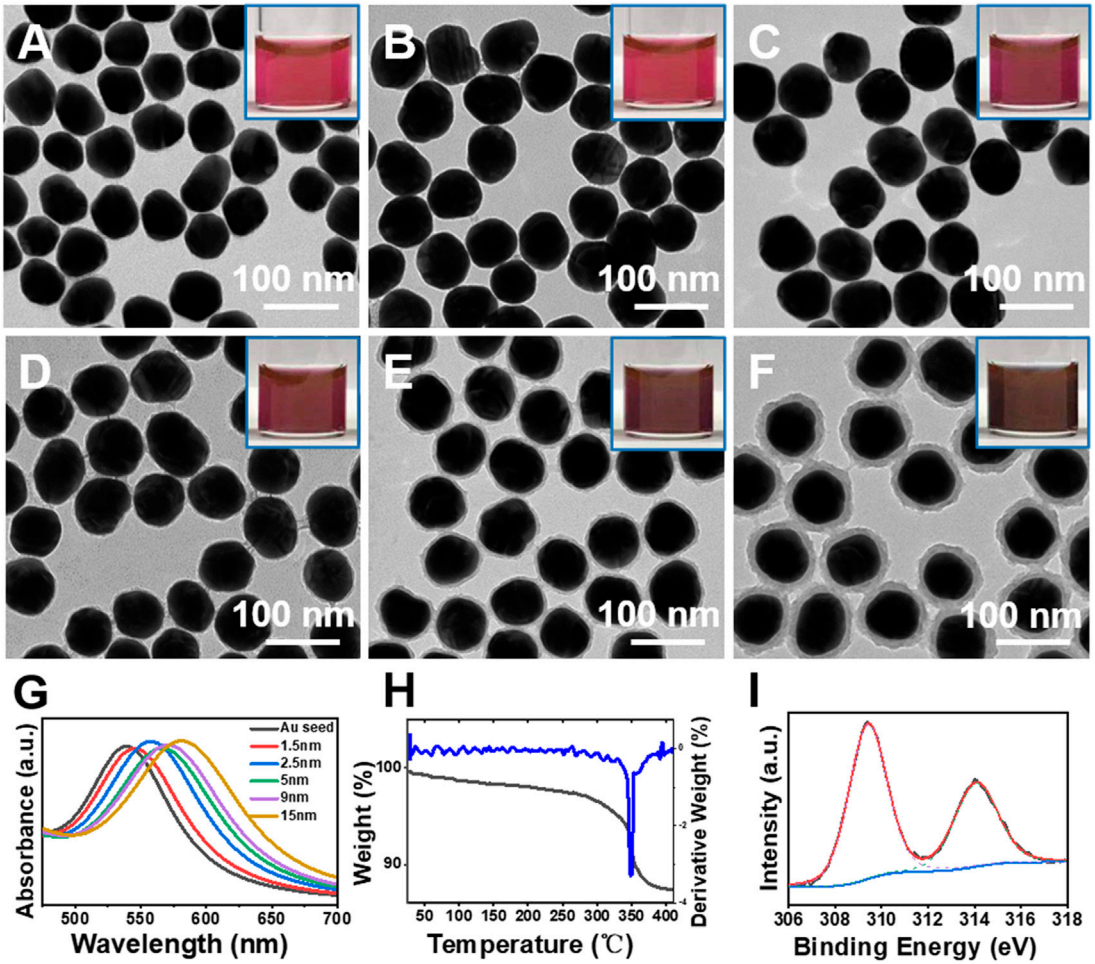

FIGURE 1
(A–F) TEM images of Au seeds and Au@$Rh(OH)_3$ core-shell structures with varying shell thickness. **(G)** Absorption, **(H)** TG and DTG curves, and **(I)** XPS spectra of the Au@$Rh(OH)_3$ structures.

L-ascorbic acid (AA) as the reductant, and $HAuCl_4$ as the precursor. In a typical synthesis, 1 mL of the Au@$Rh(OH)_3$ NPs with a 12 nm $Rh(OH)_3$ shell thickness was centrifuged and re-dispersed in 1 mL of water to remove residual chemicals. To prevent aggregation of the NPs during the growth process, 32 µl of polyvinylpyrrolidone (PVP, 2 mg/mL) was added as a surfactant under vigorous vortexing. After $HAuCl_4$ (10 mM) was added dropwise to the solution, the mixture was incubated at RT for 1 h. Subsequently, AA (10 mM) was added in one shot under vigorous vortexing. Upon the addition of AA, the color of the solution changed immediately from red to dark purple, indicating the initiation of the growth of Au on the seed NPs. The mixture was left undisturbed for 30 min for the completion of the reactions and thereafter separated for TEM/SEM characterization.

2.3.3 Synthesis of Au Island-on-[Au@$Rh(OH)_3$] structures

The synthesis of Au island-on-[Au@$Rh(OH)_3$] structures followed the same procedure as that for the synthesis of Au island-Au bridge-[Au@$Rh(OH)_3$] dumbbell structures but without pre-incubation of the Au@$Rh(OH)_3$ seeds and the $HAuCl_4$ precursor.

3 Results and discussion

For the synthesis of the Au–Au heterostructures, seeds of Au@$Rh(OH)_3$ core-shell structures with varying $Rh(OH)_3$ shell thicknesses were synthesized *via* the seed-mediated growth of $Rh(OH)_3$ on citrate-stabilized AuNPs (Figure 1, Supplementary Figures S1, S2).

As shown in Figures 1B–F, with an increase in the $RhCl_3$ and MBIA ligand (50–200 µM, Supplementary Table S1), concentric Au@$Rh(OH)_3$ core-shell structures with increasing $Rh(OH)_3$ shell thickness (1.5–18 nm) were obtained. From the enlarged TEM images, a uniform $Rh(OH)_3$ layer can be observed on the surface of the Au seeds, even with a very thin thickness (1.5 and 2.5 nm in Figures 1B, C). From the inset photographs, the color of the Au@$Rh(OH)_3$ samples changed from red to dark red and brown with an increase in the shell thickness (Figures 1A–F). The absorption peaks of the Au cores in Au@$Rh(OH)_3$ were continuously redshifted from 540 nm (Au seeds) to 544, 547, 553, 563, and 579 nm (Figure 1G). This can be attributed to the increase in the refractive index owing to the increase in the $Rh(OH)_3$ shell thickness (Yue et al., 2016; Xu et al., 2021).

The synthesis of Au@metal oxide core-shell structures has been extensively studied (Sun et al., 2013; Lukosi et al., 2016). However,

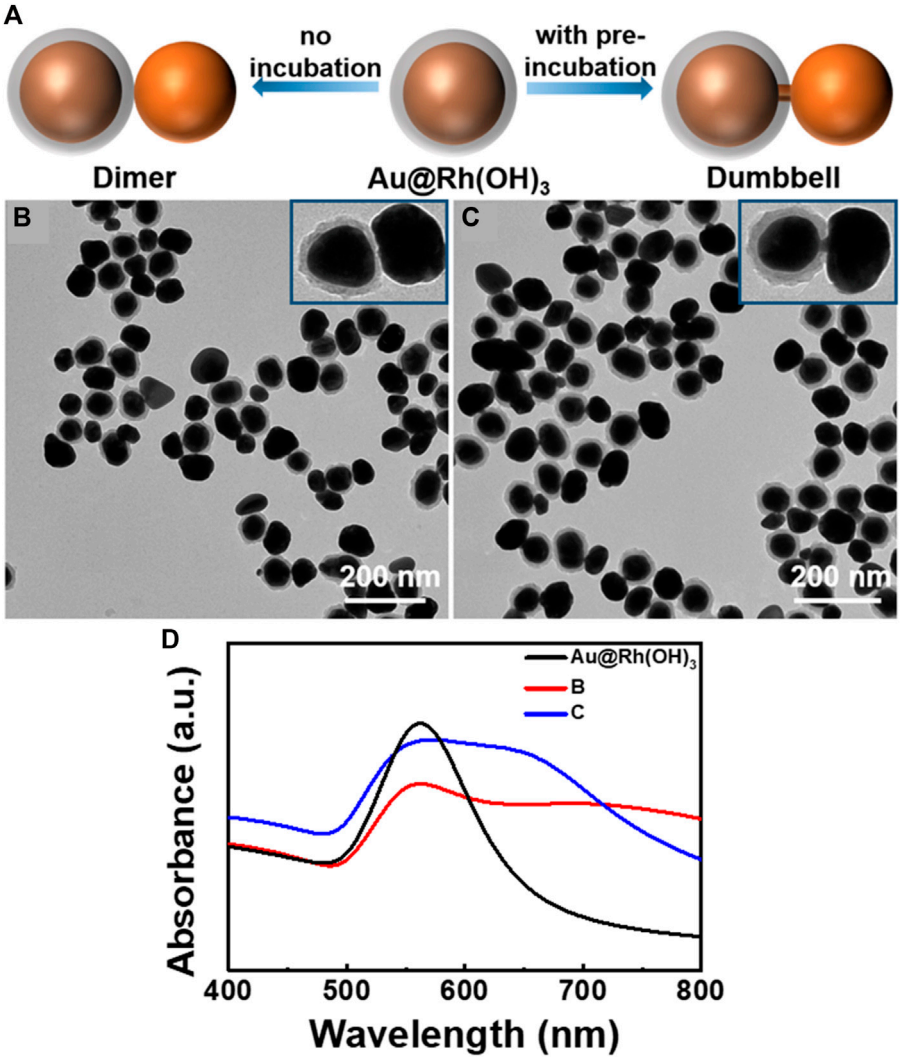

FIGURE 2
(A) Schematics illustrating the synthesis of Au-[Au@Rh(OH)$_3$] hetero-structures. TEM images of **(B)** Au island-on-[Au@Rh(OH)$_3$] dimer and **(C)** Au island-Au bridge-[Au@Rh(OH)$_3$] dumbbell structures. **(D)** Absorption spectra for the structures illustrated in Figures 2B, C.

reports on Au@metal hydroxide core-shell structures are rare because of the low compatibility and significant mismatch between Au and hydroxide materials (Zhou and Zeng, 2016; Cai et al., 2020).

In our synthesis, the Au seeds were preincubated with MBIA ligands at 60°C for 2 h prior to the growth of the Rh(OH)$_3$ shell. The MBIA ligand played dual roles in the formation of Au@Rh(OH)$_3$ core-shell NPs: 1) Modification of Au seeds with a stable MBIA layer through the strong interaction of the -SH group with Au (Feng et al., 2012). The control experiment demonstrated that without the pre-incubation of Au seeds with the MBIA ligand, a mixture of free Rh(OH)$_3$ NPs and Au seeds was observed (Supplementary Figure S3). This revealed that citrate-stabilized AuNPs are not suitable for the heterogeneous nucleation and growth of Rh(OH)$_3$ because of the high interfacial energy (the difference in surface energy, Peng and Yang, 2009; Carbone and Cozzoli, 2010) between the Au and Rh(OH)$_3$ materials. For Au@MBIA seeds, the dense -COOH groups on the surface can act as anchors for the partially hydrolyzed Rh^{3+} cations through the formation of the COO-Rh(OH)$_n$ (n < 3) complex (Kataoka et al., 2010; Enriquez Garcia and Jalilehvand, 2018), promoting the formation of Rh(OH)$_3$ shells on Au seeds. 2) The formation of the Rh^{3+}-MBIA complex in the growth solution played a vital role in the formation of the Rh(OH)$_3$ shell on the Au seeds by slowing the hydrolysis rate of Rh^{3+} ions.

XPS, TG, and DTG measurements were performed to confirm the composition of the shell material. As shown in the XPS spectrum (Figure 1), the two peaks observed at 309.4 and 314 eV can be assigned to the Rh $3d_{5/2}$ and Rh $3d_{3/2}$ peaks, respectively, confirming the +3 valency of the Rh cation (Kim and Hatfield, 1991). From the TG/DTG analysis (Figure 1H), the first mass loss (4.5%) at temperatures less than 325°C can be assigned to the loss of crystal water. The second mass loss (8.5%) in the temperature range of 325°C–350°C was due to the dehydration of Au@Rh(OH)$_3$, from which the shell was confirmed as Rh(OH)$_3$ (Schünemann et al., 1994).

For the synthesis of Au–Au hybrid nanostructures, Au–Rh(OH)$_3$ core-shell NPs with varying shell thicknesses were used as seeds, AA as the reductant, and $HAuCl_4$ as the precursor (Figure 2). In a typical synthesis, the Au@Rh(OH)$_3$ NPs were centrifuged and redispersed in the same volume of DI water, followed by the addition of PVP to

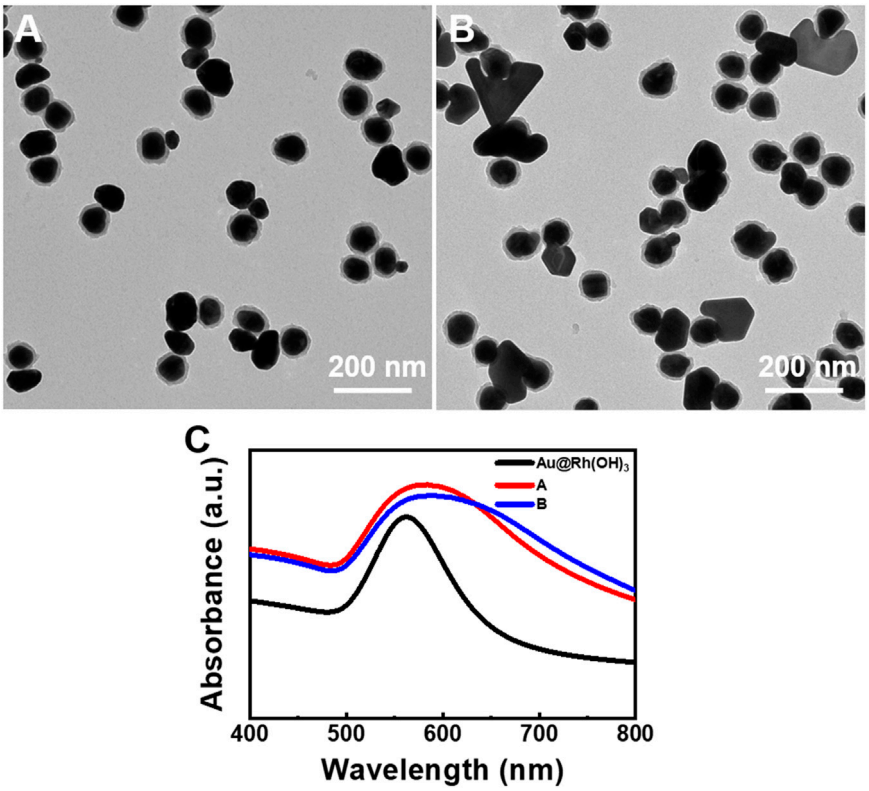

FIGURE 3
Au–Au@Rh(OH)$_3$ dimers synthesized under low AA concentration: **(A)** Without and **(B)** with pre-incubation of Au@Rh(OH)$_3$. **(C)** Absorption spectra of the structures illustrated in Figures 3A, B.

prevent the aggregation of the NPs during growth. After $HAuCl_4$ (10 mM) was added dropwise to the above solution, the mixture was incubated at RT for 1 h and thereafter, AA was added in one shot under vigorous vortexing. The mixture was left undisturbed for 30 min to complete the reaction.

As shown in Figure 2B, when Au@Rh(OH)$_3$ NPs with a shell thickness of 12 nm were used as seeds, Au island-Au@Rh(OH)$_3$ dimers were obtained. Interestingly, a thin Au bridge (approximately 12 nm in length and 6 nm in diameter) in the Rh(OH)$_3$ shell can be observed in 57% of the NPs (Figure 2C; Supplementary Figure S4), linking the Au core and the outer Au island to Au island-Au bridge-[Au@Rh(OH)$_3$] dumbbell structures with a thin "handle". Such dumbbell-shaped structures were achieved only using the physical lithography method on a solid substrate. Colloidal synthesis remains a significant challenge due to the lack of an effective control method (Koya and Lin, 2016; Wang et al., 2019a).

Because the Au island-Au bridge-[Au@Rh(OH)$_3$] dumbbell structures were grown from Au@Rh(OH)$_3$ seeds, it can be concluded that the growth startarted from the nucleation and growth of the Au bridge on the surface of the Au core in the Rh(OH)$_3$ shells. When the growth of the Au bridge penetrated the Rh(OH)$_3$ shells, an Au island formed at the end. As shown in Figure 2D, for Au@ Rh(OH)$_3$ seeds, a single absorption peak was observed at 560 nm. After the growth of the Au islands, except for the redshift of the 560 nm peak, new broad absorptions were observed at 650 and 700 nm for structures 2B and 2C, respectively. Considering the high similarity in structural parameters for structures 2B and 2C, their variance in absorption spectra should arise from the different plasmonic couplings with and without the thin Au bridge between the Au core and newly grown Au islands (Wang et al., 2017; Zhou et al., 2018; Dhiman et al., 2019).

Similar to the inorganic oxide polymer SiO_2 or TiO_2 (Song et al., 2015; Yu et al., 2021), the Rh(OH)$_3$ shell condensed from the hydrolysis of $RhCl_3$ in a basic aqueous solution should be highly porous (Supplementary Figure S5). When incubating with $HAuCl_4$, the $AuCl_4^-$ ions diffused into the pores of the Rh(OH)$_3$ shells.

It is known that the heterogeneous nucleation would occur prior the homogeneous nucleation due to its lower nucleation barrier (Wang et al., 2015). For the Au@Rh(OH)$_3$ seeds, there are two types of sites for the heterogeneous nucleation of Au: the Au cores in the Rh(OH)$_3$ shells and the surface of the Rh(OH)$_3$ shells. From the perspective of interfacial energy, the Au core should be the preferential site for the same Au material, and the surface of the Rh(OH)$_3$ shell should have a higher nucleation barrier. This variance can be reflected at different critical growth material concentrations (CGMC) needed for nucleation, that is, lower CGMC on the Au core and higher CGMC on the Rh(OH)$_3$ shell (Wang et al., 2015).

Upon the addition of the reductant AA, Au atoms can be produced where AA reaches *via* diffusion both in the growth solution and inside the pores. Therefore, the concentration of Au atoms in the solution should be higher than that in the Rh(OH)$_3$ shells as the slower diffusion of AA inside the Rh(OH)$_3$ shells. However, the lower

10.3389/fchem.2023.1138932

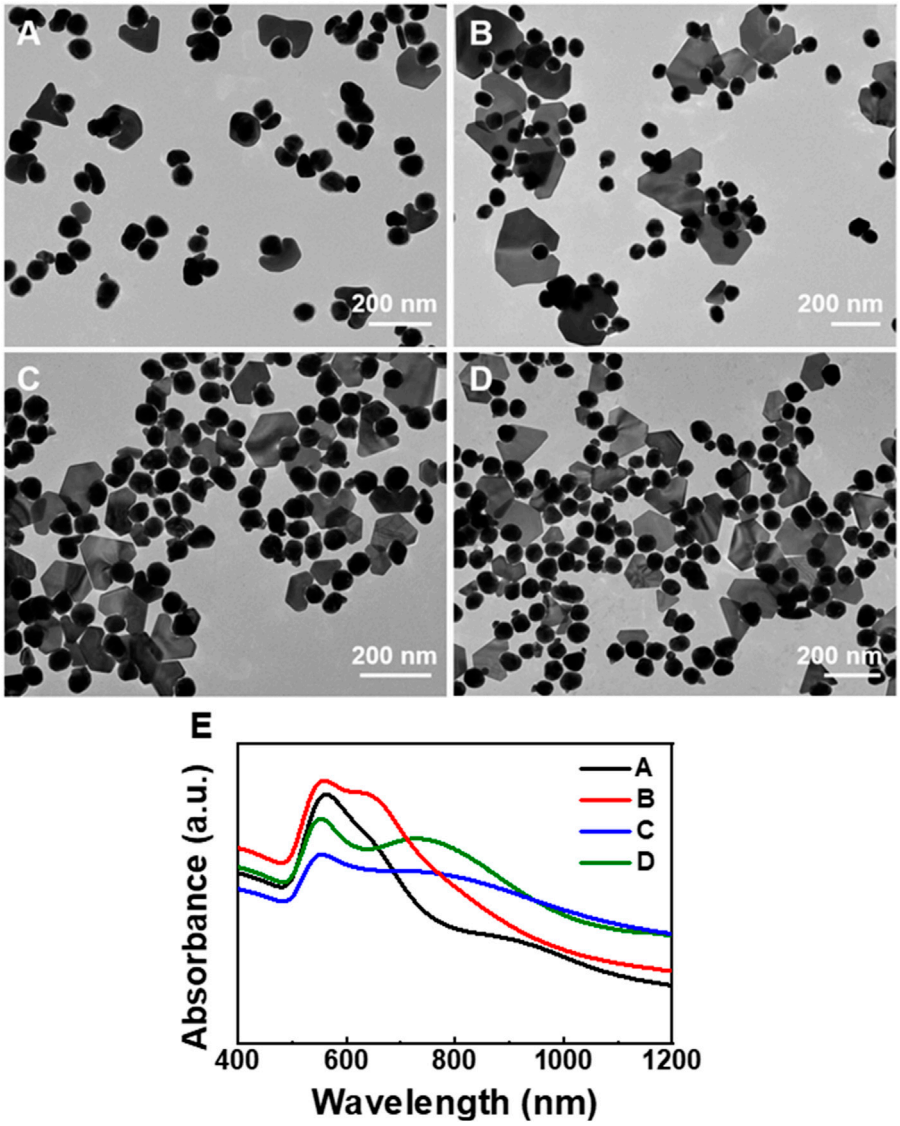

FIGURE 4
TEM images of the Au plate-Au bridge-[Au@Rh(OH)$_3$] structures synthesized using Au@Rh(OH)$_3$ seeds with **(A, B)** 8, **(C)** 5, and **(D)** 2.5 nm shell thickness. **(E)** Absorption spectra of the structures illustrated in Figures 4A–D.

nucleation barrier resulted in a lower CGMC for the nucleation on the inner Au core. Thus, the heterogeneous nucleation of Au on the Au core can occur prior to the outer Rh(OH)$_3$ shells.

Owing to the MBIA ligand layer on the Au cores, single-site nucleation of Au occurred because of the high interfacial energy between the Au@MBIA and Au deposit (Feng et al., 2012). According to the depletion sphere model (Feng et al., 2017), the formation of a nucleus depletes Au atoms (both inside and outside the Rh(OH)$_3$ shells). The low concentration of Au atoms (<CGMC) cannot support the formation of a new nucleus nearby. This is the reason why only one Au bridge on each AuRh(OH)$_3$ seed is the dominant product.

Determined by the diffusion direction of AA from the solution vertical to the Au cores, the extrusion growth of Au in the Rh(OH)$_3$ shell leads to the formation of a thin Au bridge vertical to the seed surface. When the growth of the Au bridge penetrated the Rh(OH)$_3$ shell, the end of the Au bridge grew into a spherical Au island because of the fast growth under high concentrations of Au atoms in the growth solution.

To confirm the above hypothesis, control experiments were performed under similar conditions, but without the pre-incubation of Au@Rh(OH)$_3$ seeds and HAuCl$_4$. As shown in Figure 2B, all the Au islands grew on the surface of the Rh(OH)$_3$ shells, forming Au island-on-[Au@Rh(OH)$_3$] structures. This result demonstrates that the pre-incubation of Au@Rh(OH)$_3$ and HAuCl$_4$ is the key step for the formation of a thin Au bridge. In contrast to the 1: 1 Au island-Au bridge-[Au@Rh(OH)$_3$] structures, two to three Au islands grew on each Au@Rh(OH)$_3$ seed. This multi-island growth of Au on the Au@Rh(OH)$_3$ seeds likely resulted from the fast nucleation at high Au atom concentrations (Feng et al., 2017). Without preincubation, AA was added immediately after the addition of HAuCl$_4$. Without mass loss due to diffusion into the Rh(OH)$_3$ shells, the reduction of HAuCl$_4$ at high concentrations led to increased oversaturation of Au atoms at the moment of nucleation.

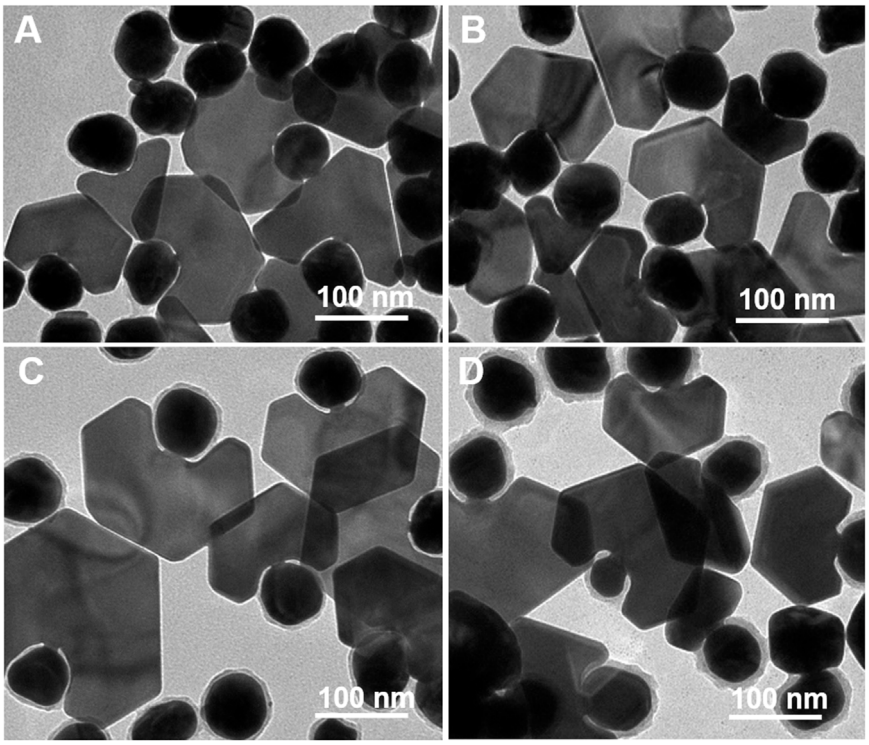

FIGURE 5
TEM images of the Au plate-Au bridge-Au@$Rh(OH)_3$ structures with different size of Au bridges synthesized using Au@$Rh(OH)_3$ seeds with varying shell thickness: **(A)** 2.5, **(B)** 5, **(C)** 8, and **(D)** 12 nm.

Thus, multi-site nucleation can occur. Based on the above conditions, when the concentration of AA was reduced from 0.7 to 0.4 mM, single-island growth of Au on the surface of the Au@$Rh(OH)_3$ seeds was observed (Figure 3A), confirming the reduction rate effect during nucleation.

With pre-incubation, a lower [AA] led to the formation of Au island-Au@$Rh(OH)_3$ (80%) and Au plate-Au@$Rh(OH)_3$ dimers (20%) (Figure 3B). The enlarged TEM images (Supplementary Figure S6) demonstrate that the Au island domains in the Au island-Au@$Rh(OH)_3$ dimers are thick Au bridges grown on the Au core. Because the surface area of the end of the Au bridge is very large, when it penetrates the $Rh(OH)_3$ shell, the insufficient supply of Au atoms cannot support the formation of Au islands. Therefore, unlike the thin Au bridge, no Au islands are formed at the end of the Au bridge. As shown in Figure 3C, a single broad absorption in the wavelength range of 500–800 nm was observed for both structures 3A and 3B. In comparison to structure 3A, the slight redshift and clear broadening of the absorption for structure 3B may be due to the formation of more new Au domains in plate shapes. It should be noted that due to the relative low uniformity of the Au-Au structures, the measured absorption is the ensembled average absorptions of the mixed structures, which cannot be precisely assigned in analysis.

It is well known that the synergistic effect of the presence of the twin plane and selective ligand blocking of the Au 111 surface is responsible for the formation of the Au nanoplate. PVP is known as a surface-blocking agent for the synthesis of Au nanoplates because of its strong coordination on the Au 111 surface (Wang et al., 2010; Wang et al., 2016; Balasubramanian and Raghavachari, 2017). Thus, we speculate that the coexistence of the Au island-Au@$Rh(OH)_3$ and Au plate-Au@$Rh(OH)_3$ structures is due to the random twinning during the growth of the Au bridges. The Au bridges without twin planes grew into Au islands (thick bridges), whereas those with twin planes vertical to the surface of the Au cores grew into Au nanoplates after they penetrated the $Rh(OH)_3$ shells. As shown in Figure 3B, the size of the Au plates is significantly larger than that of the Au islands in Au–Au dimers. This was due to the fast growth of Au at the concave defect site of the twin plane (Jiang et al., 2018).

Interestingly, when Au@$Rh(OH)_3$ seeds with thinner shells (8 nm) were pre-incubated with $HAuCl_4$, the growth of Au nanoplates with higher purity (approximately 33%) was observed. At a lower AA (0.4 mM), the purity of the Au plate-Au bridge-[Au@$Rh(OH)_3$] structure was further increased to 37% (Figures 4A, B). When the thickness of the $Rh(OH)_3$ shell was further decreased to 5 nm and 2.5 nm, the purity of Au plate-Au bridge-[Au@$Rh(OH)_3$] structures continuously increased slightly (40% and 44%, respectively). From the absorption spectra shown in Figure 4E, with the decrease in the $Rh(OH)_3$ shells, the transverse absorption of Au continuously blue-shifted from 563 to 560, 554, and 553 nm owing to the decrease in the refractions of $Rh(OH)_3$. In addition, with an increase in the plate-shaped Au domains, the longitudinal absorptions for structures A–D changed from shoulder peaks (A and B) to single broad absorptions. The continuous redshift (from 638 to 643, 738, and 766 nm) was a result of the increase in the structural anisotropy and LSPRs coupling between the Au core and outer Au nanoplates (Feng and Chen, 2021).

When the shell thickness was greater than 12 nm, the Au island-Au bridge-[Au@$Rh(OH)_3$] structure became the

dominant product. In addition, the yield decreased with increasing shell thickness (Supplementary Figure S7). A possible reason for this observation is that because of the longer diffusion path of AA from the solution to the inner Au core, the nucleation of Au on the surface of the $Rh(OH)_3$ shell may occur first, leading to the formation of the Au island-on-[Au@$Rh(OH)_3$] structure. The thicker the $Rh(OH)_3$ shell, the higher the yield of the Au island-on-[Au@$Rh(OH)_3$] structure (Supplementary Figure S7).

When the shell thickness is different, except for the different purities of the products, the sizes of the Au bridges also differ. The enlarged TEM images illustrated in Figure 5 show that when the thickness of the $Rh(OH)_3$ shell increased from 2.5 to 5, 8, and 12 nm, the length of the Au bridges increased from 2.5 to 3.5, 5.5, and 8 nm, and the width increased from 3 to 7, 8.5, and 12 nm, respectively. It is reasonable to assume that the length of the Au bridges is determined by the thickness of the $Rh(OH)_3$ shell. The width of Au bridges is highly dependent on their length. Generally, the growth of an Au bridge in the vertical and lateral directions occurs simultaneously. With an increase in length, the width also continuously increased owing to the longer growth time. From the HRTEM analysis, the Au plate and Au bridge are epitaxially grown from the surface of the Au seeds (Supplementary Figure S9).

4 Conclusion

In conclusion, we developed a new method for synthesizing bridged Au–Au dumbbell structures by controlling the diffusion of the $HAuCl_4$ precursor in the porous $Rh(OH)_3$ shell of Au@$Rh(OH)_3$ seeds. While the pre-incubation of the Au@$Rh(OH)_3$ seeds and $HAuCl_4$ is a prerequisite for the formation of Au bridges in $Rh(OH)_3$ shells, the thickness of the $Rh(OH)_3$ shells and the concentration of AA reductant can both affect the formation of Au bridges and the shape of the end Au domains, respectively. Importantly, the growth of the Au bridge was completely different from the conventional wetting growth of Au on Au seeds. In the porous $Rh(OH)_3$ shells, the extrusion growth of Au inhibited their wetting of Au seeds. We believe that this new diffusion control approach will create new approaches for achieving site-specificity in colloidal synthesis, which would eventually promote the synthesis of new sophisticated functional nanomaterials.

Data availability statement

The original contributions presented in the study are included in the article/Supplementary Materials, further inquiries can be directed to the corresponding authors.

Author contributions

JZ and QR performed the syntheses and characterizations of the Au-Au heterostructures, RX participated in the data analysis and discussion, YW helped with the control experiments and created the artwork, HC helped with the discussion of the mechanism, YF and WX designed the study and wrote the manuscript.

Funding

This work was supported by the Jiangsu Science and Technology Plan (BK20211258), Nanjing Tech University (39837140), and Jiangsu Funding Program for Excellent Postdoctoral Talen.

Conflict of interest

The authors declare that the research was conducted in the absence of any commercial or financial relationships that could be construed as a potential conflict of interest.

Publisher's note

Supplementary material

The Supplementary Material for this article can be found online at: https://www.frontiersin.org/articles/10.3389/fchem.2023.1138932/full#supplementary-material

References

Bai, S., Sun, Y., Yi, J., He, Y., Qiao, Y., and Zhou, H. (2018). High-power Li-metal anode enabled by metal-organic framework modified electrolyte. *Joule* 2 (10), 2117–2132. doi:10.1016/j.joule.2018.07.010

Balasubramanian, S., and Raghavachari, D. (2017). Green synthesis of triangular Au nanoplates: Role of small molecules present in bael gum. *ACS Sustain. Chem. Eng.* 5 (11), 10317–10326. doi:10.1021/acssuschemeng.7b02346

Cai, R., Jin, H., Yang, D., Lin, K.-T., Chan, K., Sun, J., et al. (2020). Generalized preparation of Au NP @ $Ni(OH)_2$ yolk-shell NPs and their enhanced catalytic activity. *Nano Energy* 71, 104542. doi:10.1016/j.nanoen.2020.104542

Campodoni, E., Patricio, T., Montesi, M., Tampieri, A., Sandri, M., and Sprio, S. (2018). "3 - biomineralization process generating hybrid nano- and micro-carriers," in *Core-shell nanostructures for drug delivery and theranostics*. Editors M. L. Focarete and A. Tampieri (Woodhead Publishing), 19–42.

Carbone, L., and Cozzoli, P. D. (2010). Colloidal heterostructured nanocrystals: Synthesis and growth mechanisms. *Nano Today* 5 (5), 449–493. doi:10.1016/j.nantod.2010.08.006

Chen, Y., Feng, Y., Deveaux, J. G., Masoud, M. A., Chandra, F. S., Chen, H., et al. (2019). Biomineralization forming process and bio-inspired nanomaterials for biomedical application: A review. *Minerals* 9 (2), 68. doi:10.3390/min9020068

Crossland, E. J. W., Noel, N., Sivaram, V., Leijtens, T., Alexander-Webber, J. A., and Snaith, H. J. (2013). Mesoporous TiO_2 single crystals delivering enhanced mobility and optoelectronic device performance. *Nature* 495 (7440), 215–219. doi:10.1038/nature11936

Dhiman, M., Maity, A., Das, A., Belgamwar, R., Chalke, B., Lee, Y., et al. (2019). Plasmonic colloidosomes of black gold for solar energy harvesting and hotspots directed catalysis for CO_2 to fuel conversion. *Chem. Sci.* 10 (27), 6594–6603. doi:10.1039/c9sc02369k

Enriquez Garcia, A., and Jalilehvand, F. (2018). Aerobic reactions of antitumor active dirhodium(II) tetraacetate $Rh_2(CH_3COO)_4$ with glutathione. *JBIC J. Biol. Inorg. Chem.* 23 (2), 231–239. doi:10.1007/s00775-017-1524-6

Feng, Y., and Chen, H. (2021). "Design and synthesis of plasmonic nanoparticles," in *World scientific reference on plasmonic nanomaterials principles, design and bio-applications volume 1: Principles of nanoplasmonics*. Editor J-M. Nam (Korea: Seoul National University, World Scientific), 31–84.

Feng, Y., He, J., Wang, H., Tay, Y. Y., Sun, H., Zhu, L., et al. (2012). An unconventional role of ligand in continuously tuning of metal–metal interfacial strain. *J. Am. Chem. Soc.* 134 (4), 2004–2007. doi:10.1021/ja211086y

Feng, Y., Wang, Y., Song, X., Xing, S., and Chen, H. (2017). Depletion sphere: Explaining the number of Ag islands on Au nanoparticles. *Chem. Sci.* 8 (1), 430–436. doi:10.1039/C6SC02276F

Jiang, T., Chen, G., Tian, X., Tang, S., Zhou, J., Feng, Y., et al. (2018). Construction of long narrow gaps in Ag nanoplates. *J. Am. Chem. Soc.* 140 (46), 15560–15563. doi:10.1021/jacs.8b06969

Kataoka, Y., Kitagawa, Y., Saito, T., Nakanishi, Y., Matsui, T., Sato, K., et al. (2010). Theoretical study on the electronic configurations and nature of chemical bonds of dirhodium tetraacetato complexes $[Rh_2(CH_3COO)_4(L)_2]$ (L = H_2O, free): Broken symmetry approach. *Bull. Chem. Soc. Jpn.* 83 (12), 1481–1488. doi:10.1246/bcsj.20100128

Kim, Y. I., and Hatfield, W. E. (1991). Electrical, magnetic and spectroscopic properties of tetrathiafulvalene charge transfer compounds with iron, ruthenium, rhodium and iridium halides. *Inorg. Chim. Acta* 188 (1), 15–24. doi:10.1016/s0020-1693(00)80911-1

Koya, A. N., and Lin, J. (2016). Bonding and charge transfer plasmons of conductively bridged nanoparticles: The effects of junction conductance and nanoparticle morphology. *J. Appl. Phys.* 120 (9), 093105. doi:10.1063/1.4962133

Li, H., Xin Huolin, L., Muller David, A., and Estroff Lara, A. (2009). Visualizing the 3D internal structure of calcite single crystals grown in agarose hydrogels. *Science* 326 (5957), 1244–1247. doi:10.1126/science.1178583

Lukosi, M., Zhu, H., and Dai, S. (2016). Recent advances in gold-metal oxide core-shell nanoparticles: Synthesis, characterization, and their application for heterogeneous catalysis. *Front. Chem. Sci. Eng.* 10 (1), 39–56. doi:10.1007/s11705-015-1551-1

Peng, Z., and Yang, H. (2009). Designer platinum nanoparticles: Control of shape, composition in alloy, nanostructure and electrocatalytic property. *Nano Today* 4 (2), 143–164. doi:10.1016/j.nantod.2008.10.010

Schünemann, V., Adelman, B., and Sachtier, W. M. H. (1994). Formation of the rhodium oxides Rh_2O_3 and RhO_2 in Rh/NaY. *Catal. Lett.* 27 (3), 259–265. doi:10.1007/BF00813911

Shen, K., Zhang, L., Chen, X., Liu, L., Zhang, D., Han, Y., et al. (2018). Ordered macro-microporous metal-organic framework single crystals. *Science* 359 (6372), 206–210. doi:10.1126/science.aao3403

Song, X., Ding, T., Yao, L., Lin, M., Siew Tan, R. L., Liu, C., et al. (2015). On the origin and underappreciated effects of ion doping in silica. *Small* 11 (34), 4351–4365. doi:10.1002/smll.201500539

Sun, H., He, J., Wang, J., Zhang, S.-Y., Liu, C., Sritharan, T., et al. (2013). Investigating the multiple roles of polyvinylpyrrolidone for a general methodology of oxide encapsulation. *J. Am. Chem. Soc.* 135 (24), 9099–9110. doi:10.1021/ja4035335

Tampieri, A., Sprio, S., Sandri, M., and Valentini, F. (2011). Mimicking natural bio-mineralization processes: a new tool for osteochondral scaffold development. *Trends Biotechnol.* 29 (10), 526–535. doi:10.1016/j.tibtech.2011.04.011

Wang, C., Kan, C., Zhu, J., Zeng, X., Wang, X., Li, H., et al. (2010). Synthesis of high-yield gold nanoplates: Fast growth assistant with binary surfactants. *J. Nanomater.* 2010, 1–9. doi:10.1155/2010/969030

Wang, Y., He, J., Liu, C., Chong, W. H., and Chen, H. (2015). Thermodynamics versus kinetics in nanosynthesis. *Angew. Chem. Int. Ed. Engl.* 54 (7), 2022–2051. doi:10.1002/anie.201402986

Wang, G., Tao, S., Liu, Y., Guo, L., Qin, G., Ijiro, K., et al. (2016). High-yield halide-free synthesis of biocompatible Au nanoplates. *Chem. Commun.* 52 (2), 398–401. doi:10.1039/C5CC07957H

Wang, G., Liu, Y., Gao, C., Guo, L., Chi, M., Ijiro, K., et al. (2017). Island growth in the seed-mediated overgrowth of monometallic colloidal nanostructures. *Chem* 3 (4), 678–690. doi:10.1016/j.chempr.2017.08.004

Wang, T., Dong, Z., Koay, E. H. H., and Yang, J. K. W. (2019a). Surface-enhanced infrared absorption spectroscopy using charge transfer plasmons. *ACS Photonics* 6 (5), 1272–1278. doi:10.1021/acsphotonics.9b00229

Wang, T., Salvatierra, R. V., and Tour, J. M. (2019b). Detecting Li dendrites in a two-electrode battery system. *Adv. Mater* 31 (14), e1807405. doi:10.1002/adma.201807405

Wang, C., Li, C., Liu, J., and Guo, C. (2021). Engineering transition metal-based nanomaterials for high-performance electrocatalysis. *Mater. Rep. Energy* 1 (1), 100006. doi:10.1016/j.matre.2021.01.001

Xu, W., Chen, S., Xiao, R., Zong, J., Feng, Y., and Chen, H. (2021). Engineering the spatial arrangement of Au–C_{60} heterostructures. *Chem. Mater.* 33 (13), 5268–5275. doi:10.1021/acs.chemmater.1c01360

Yang, F., Hegh, D., Song, D., Zhang, J., Usman, K. A. S., Liu, C., et al. (2022). Synthesis of nitrogen-sulfur co-doped Ti_3C_2T MXene with enhanced electrochemical properties. *Mater. Rep. Energy* 2 (1), 100079. doi:10.1016/j.matre.2022.100079

Yu, Y., Yan, M., Dong, W.-D., Wu, L., Tian, Y.-W., Deng, Z., et al. (2021). Optimizing inner voids in yolk-shell TiO_2 nanostructure for high-performance and ultralong-life lithium-sulfur batteries. *Chem. Eng. J.* 417, 129241. doi:10.1016/j.cej.2021.129241

Yue, Z., Cai, B., Wang, L., Wang, X., and Gu, M. (2016). Intrinsically core-shell plasmonic dielectric nanostructures with ultrahigh refractive index. *Sci. Adv.* 2 (3), e1501536. doi:10.1126/sciadv.1501536

Zhou, Y., and Zeng, H. C. (2016). Metal–hydroxide and gold–nanocluster interfaces: Enhancing catalyst activity and stability for oxygen evolution reaction. *J. Phys. Chem. C* 120 (51), 29348–29357. doi:10.1021/acs.jpcc.6b11102

Zhou, J., Jiang, Y., Hou, S., Upputuri, P. K., Wu, D., Li, J., et al. (2018). Compact plasmonic blackbody for cancer theranosis in the near-infrared II window. *ACS Nano* 12 (3), 2643–2651. doi:10.1021/acsnano.7b08725